Robust climate responses to extreme solar minimum forcing and their hemispheric differences

Han-Li Liu[1], Matthias Rempel[1], Gokhan Danabasoglu[2], Stanley C. Solomon[1]and Joseph M. McInerney[1]

[1]High Altitude Observatory, National Center for Atmospheric Research, Boulder, Colorado, USA
[2]Climate and Global Dynamics, National Center for Atmospheric Research, Boulder, Colorado, USA

Key Points:

- Extreme solar minimum forcing simulations reveal robust climate responses.
- Hemispheric differences in the interplay between dynamical and radiative processes identified.
- Quantify tropospheric/surface and stratospheric responses that are mutually enhancing or offsetting.

Corresponding author: H.-L. Liu, liuh@ucar.edu

Abstract

Fundamental understanding of the climate responses to solar variability is obscured by the large and complex climate variability. This long-standing issue is addressed here by examining climate responses under an extreme solar minimum (ESM) scenario, obtained by making the sun void of all magnetic fields. It is used to drive a whole atmosphere climate model with coupled ocean. The simulations reveal robust responses in the coupled climate system, and elucidate similarities and differences of responses to bottom-up and top-down forcing. Planetary waves (PWs) play a key role in both regional climate and the mean circulation changes. Responses of the largest scale PW during NH and SH winters differ, leading to hemispheric differences in the interplay between dynamical and radiative processes. The analysis exposes remarkable general similarities between climate responses in ESM simulations and those under nominal solar minimum conditions, even though the latter may not appear to be statistically significant.

Plain Language Summary

Understanding how climate may change under different solar conditions is both interesting and important. However it is difficult to clearly identify solar signal from the very large climate variability on broad time scales. In this study, we tackle this problem by providing a lower bound of the solar minimum condition according to our current understanding of solar physics. By specifying this extremely low solar minimum condition in a climate model that takes into consideration of the effects of ocean and middle atmosphere, we are able to identify robust climate responses, which are very different between the northern and southern hemispheres. We gain an understanding of the processes driving these responses, including how the lower and upper atmospheric processes may enhance/offset each other. By comparing these climate responses to those under nominal solar minimum conditions, we expose climate patterns that are hidden under the large climate variability in the latter.

1 Introduction

The Sun is the ultimate driver of the Earth atmosphere system, and it is of great interest to explore the impacts of solar variability on the atmosphere on time scales ranging from solar flares to multiple solar cycles (Gray et al., 2010). While the solar signal in the stratosphere and above is clear with the large variability at ultraviolet (UV) and shorter wavelengths (Marsh et al., 2007), it is much weaker in the troposphere and at the Earth surface, with global mean surface temperature variation less than 0.1K (Gray et al., 2010), consistent with the $\lesssim$0.1% change of total solar irradiance (TSI) over a solar cycle. Regional climate, on the other hand, may respond more strongly (Meehl et al., 2009; Ineson et al., 2011; Gray et al., 2016), and feedback and amplification mechanisms have been postulated (Haigh, 1996; Kodera & Kuroda, 2002; Kodera & Shibata, 2006; Matthes et al., 2006; Meehl et al., 2009; Chiodo et al., 2012; Théblemont et al., 2015). However, the robustness of the solar signal in regional climate is still being debated (Chiodo et al., 2019), and it is challenging to establish a pathway by which the solar variability can affect the regional climate, and to understand climate sensitivity to solar forcing. One strategy to address the challenge is to increase the solar variability signal by hypothetically increasing the TSI or SSI variability (Meehl et al., 2013; Maycock et al., 2015; Ineson et al., 2015), though the SSI changes employed are not constrained by the underlying solar physics. Constraint has been suggested from historical solar irradiance (e.g. during Maunder Minimum), however, reconstruction methods suffer from large uncertainties (Shapiro et al., 2011; Schrijver et al., 2011). In this study, we will address this challenge by adapting a solar forcing that would result from a solar photosphere without magnetic field, produced by a non-magnetic, hydrodynamic (HD) solar simulation. While such a scenario is not a likely representation of a grand minimum, it is the most

extreme solar minimum (ESM) scenario that is possible within the limits set by the physics of the solar photosphere. More extreme forcing would require deeper seated changes in the stellar structure of the Sun.

2 Methods

2.1 Numerical Simulation of Quiet Sun Scenarios and Irradiance

Recently Rempel (2020) computed models of the quiet Sun, i.e. solar granulation with a mixed polarity small-scale magnetic field, in order to quantify the sensitivity of TSI and SSI to the strength of the quiet Sun magnetic field. In these models the mixed polarity magnetic field is maintained by a small-scale turbulent dynamo that was first studied in a solar-like setup by Vögler and Schüssler (2007) and later refined by Rempel (2014, 2018). In particular the latter demonstrated that the saturation field strength is dependent on the formulation of the bottom boundary that parametrizes the coupling of the photosphere to the deeper convection zone. Rempel (2020) took advantage of this boundary dependence in order to create quiet Sun models with varying field strengths: A non-magnetic, hydrodynamic (HD) reference, a current quiet sun reference (small-scale dynamo with ∼67G vertical magnetic field strength at optical depth of unity – SSD67), a "low-activity" quiet sun (∼ 44G field vertical strength – SSD44) as well as a "high-activity" quiet sun (∼86 G vertical field strength – SSD86). It is noted that these values are slightly different from those reported in (Rempel, 2020): the former are obtained from averaging 6-16 hours of the simulation, while the latter are from 6-30 hours of the simulations. The slight difference between them is due to model intrinsic fluctuations in both field strength and resulting radiative properties. Comparing these simulations (Rempel, 2020) found a TSI sensitivity of about 0.14% per 10G of unsigned flux in the photosphere. This rather high TSI sensitivity implies that only a moderate change of the quiet Sun by 10% in field strength would cause a TSI variation comparable to the observed solar cycle TSI variability.

In addition to the TSI, Rempel (2020) also computed SSI in the 200 - 10,000 nm spectral range using Kurucz/Castelli Opacity Distribution Functions (ODFs) (see Rempel (2020) for further detail). We use from Rempel (2020) the models HD and SSD67 to derive the most extreme solar minimum forcing consistent with physics of the solar photosphere by computing the SSI change that is expected from removing all magnetic fields in the solar photosphere. We emphasize that this is not a likely scenario for a grand solar minimum, and serves in this study solely as an extreme forcing to highlight subtle differences in the climate response that are easily hidden by the natural climate variability. Since Rempel (2020) computed SSI only for the range from 200-10,000 nm, between 121nm (Lyman-alpha) and 200nm the SSI is deduced from an empirical scaling relationship. TSI from SSD67 simulation (current quiet sun reference) is not exactly equal to the TSI of the nominal solar minimum used in our climate simulations. In order to make meaning comparisons between the climate simulations, SSI values of HD, SSD44 and SSD67 are further scaled by multiplying a scaling factor, TSI(Smin)/TSI(SSD67). With this scaling, the corresponding TSI for HD and SSD44 are 1350.08 Wm^{-2} and 1354.83 Wm^{-2}, 0.77% and 0.42% lower than the nominal solar minimum TSI value (also the scaled SSD67 value) (1360.43 Wm^{-2}).

2.2 Whole Atmosphere Community Climate Model and Numerical Experiments

The Whole Atmosphere Community Climate Model (WACCM) is one of the atmosphere components of the NCAR Community Earth System Model version 1.1 (CESM 1.1) with its upper boundary extended to the lower thermosphere (∼140 km). The WACCM configuration used in this study is the same as that employed for the Chemistry-Climate Model Initiative (CCMI). As described in Morgenstern et al. (2017), this version of WACCM

includes chemistry packages for the troposphere and stratosphere (Tilmes et al., 2016; Wegner et al., 2013) and for the mesosphere and lower thermosphere (Marsh et al., 2013). It also includes an updated gravity wave parameterization scheme which leads to improved model climatology (Garcia et al., 2017). The CESM/WACCM for this study includes the fully coupled Parallel Ocean Program (POP) ocean component (Danabasoglu et al., 2012). All WACCM simulations discussed in this study are with coupled ocean component. The horizontal resolution of WACCM for the simulation is $1.9^\circ \times 2.5^\circ$ in latitude and longitude, and there are 66 vertical levels. The horizontal resolution of POP is $\sim 1^\circ$.

CESM/WACCM simulations are first performed under nominal solar maximum (TSI: 1361.93 Wm^{-2}, referred as Smax run) and solar minimum (TSI: 1360.43 Wm^{-2}, Smin) conditions. Both sets of simulations are initialized by the same equilibrated pre-industrial control simulation, and the emission level is held constant during the 200-year simulation. The annually averaged global mean surface temperature from Smax and Smin simulations are shown in Supporting Information Figure S1.

CESM/WACCM simulations are then performed using the SSI and TSI from the HD solar simulation, with the same initial condition as Smax and Smin, and the simulation length is 200 years. In order to further differentiate the effects by solar heating near the Earth surface and by the ozone heating in the stratosphere, two additional simulations have been performed: in HDVIR the SSI at wavelengths longer than 320 nm is taken from the HD SSI while at shorter wavelengths the SSI is the same as in Smin; in HDUV the SSI at wavelengths shorter than 320 nm is taken from HD SSI while at longer wavelengths the SSI the same as in Smin. The TSI for HDVIR and HDUV are 1350.84 Wm^{-2} and 1359.76 Wm^{-2}, respectively. The initialization and length of the simulations are the same as HD. It is noted that CESM/WACCM simulations have also been performed using TSI and SSI from the low-activity quiet sun (SSD44), and the results are qualitatively similar to the HD results.

A summary of the CESM/WACCM simulations with different solar forcing is presented in Table 1. The climate sensitivity is calculated with respect to Smax, $(T_s - T_s(Smax))/(TSI - TSI(Smax))$, for each set of the solar minimum simulations over years 50–200.

3 Results

CESM/WACCM simulations have been performed under such ESM conditions, under nominal solar maximum and minimum conditions, as well as with only the visible and infrared (VIR) or ultraviolet (UV) part of the SSI changed to that from the ESM conditions. The annual averages of the global mean surface temperature (T_s) from the Smax, HD, HDVIR, and HDUV simulations are shown in Fig. 1(a), with T_s of HD, HDVIR, and HDUV lower than Smax by 0.833, 0.79, and 0.149 K, respectively, more than the cooling of Smin (0.087 K, Figure S1). The time for T_s to reach quasi-equilibrium differs in northern hemisphere (NH, 30-90°N), southern hemisphere (SH, 30-90°S) and at low latitudes: several years in NH and about 3 decades in SH and at low latitudes (Fig. 1 (b-d)). In most of the analysis, climatologies from the last 150 years of the HD, HDVIR, HDUV, and Smin simulations are compared with the Smax simulations.

3.1 Surface temperature patterns in response to solar forcing changes

Global patterns of T_s differences between HD/HDVIR and Smax for northern and southern winter seasons (DJF and JJA respectively) show significant cooling throughout most of the globe (Fig. 1(e and i), (f and j)), with the most pronounced cooling found in the Arctic, over Eurasia and North America (especially their northeast coastal regions), and the Antarctic (especially its coastal region in the south Indian Ocean sector) during their respective winter seasons. In particular, sea ice growth is noted in the western Bering Sea and the Southern Ocean with the strongest cooling. The coastal cooling co-

incides generally with regions with the largest upward sensible heat flux (da Silva et al., 1995), suggesting strong heat loss to the air blowing from the continents, which are colder due to the reduced solar activity. The strong atmosphere cooling over the Arctic also leads to the thickening of sea-ice, which results in brine rejection in the ocean, making the Arctic saltier and denser. The dense water finds its way into the deep northern North Atlantic around 1000-m depth, and pushes the North Atlantic Deep Water (NADW) cell deeper without much change in the upper ocean or northward heat transport (Supporting Information Figure S2). At lower latitudes, the cooling over continents is generally more pronounced than over the ocean for both seasons. A notable exception is the significant cooling over the tropical central eastern Pacific, and this is in contrast to the previous report of tropical eastern Pacific cooling during peak solar years (Meehl et al., 2009). In contrast to the overall cooling, there is a distinct warm anomaly in the central North Atlantic region in HD and HDVIR (up to ∼0.5 K during DJF).

Similar spatial patterns are noted in the surface temperature changes in HDUV (Fig. 1(g and k)), albeit with smaller magnitude in comparison with HD and HDVIR. Coolings of 0.6–0.8 K and ∼0.4 K over NH continents and equatorial central eastern Pacific are one half and one third, respectively, of those in HDVIR. A prominent warm anomaly is found during JJA extending from Weddell Sea to Ross Sea. While there is no net warming at that location in HD/HDVIR, probably because it is offset by the strong surface cooling, a similar zonal wavenumber 1 structure is noted. The similarities between the HDUV and HDVIR underscore responses that are enhanced by the solar forcing changes in the stratosphere and in the troposphere/surface. As such, similar patterns are also seen in the surface temperature difference between Smin and Smax (e.g. cooling of 0.4–0.5K over NH continents and 0.3K over central eastern Pacific).

3.2 Regional changes of tropospheric winds and air-sea interaction

Surface and regional climate changes are closely associated with tropospheric winds, which are found to respond significantly to solar forcing changes (Fig. 2). At 300 hPa, the meridional wind changes during boreal winter display a robust pattern in the NH that is remarkably similar (with opposite signs) to the stationary wave changes in response to a warming climate (Simpson et al., 2016; Wills et al., 2019). This reflects perturbations to the circumglobal teleconnection pattern and is caused mainly by the weakening of the eastward tropospheric wind (Fig. 4) (Branstator, 2002; Simpson et al., 2016), which alters the dominant length scale of stationary waves that are supported by the subtropical wave guide. The slower zonal wind also leads to the decreases of the propagation speed of the PWs, and is likely responsible for the equatorward shift of large-scale PWs. Similar stationary wave patterns are seen in all four solar minimum simulations (Supporting Information Figure S3(i-p)). By comparing the Smin and HD results, therefore, we can identify robust regional climate responses that may not appear statistically significant in the former. For example, regional cooling and drying by equatorward winds over Europe, Middle East, East Asia, western North America, southern Africa, and South America are likely robust features during solar minimum (Fig. 1(h and l), Supporting Information Figure S3(l and p)).

In addition to the regional changes over major continents, northward/eastward wind anomaly is seen over the North Atlantic at both 300 hPa and 850 hPa, most significant during boreal winter (Fig. 2). This change enhances the north-eastward ocean circulation, thus causes the prominent warming of the central North Atlantic Ocean as seen in surface temperature (Fig. 1). It is also seen that the trade wind over the central eastern Pacific is enhanced, suggesting an enhancement of the Walker circulation, leading to cooling over the tropical eastern Pacific (Fig. 1). This is probably caused by the increasing lapse rate (Fig. 4(b,d))–thus enhanced convection–in the troposphere. This is a robust feature seen in all cases, again suggesting the troposphere/surface and stratospheric responses are mutually enhancing. This change appears to offset the weakening

of Walker circulation under solar minimum forcing (Meehl et al., 2009), and is consistent with the recent finding of a slower Walker circulation at solar maximum (Misios et al., 2019).

During austral winter (and spring), the strongest zonal wind deceleration can extend down to the surface at mid to high latitudes (Fig. 3). At 54°S this is most significant around 0° and 45°W in HD and HDUV respectively. Changes with similar longitude-height structures are found in all four solar minimum cases, with different levels of significance. The westward wind anomaly near the surface induces a poleward Ekman transport and thus a warm anomaly around Weddell Sea. This is most evident in HDUV case, both because of the significant westward wind change and the lack of strong surface cooling.

3.3 Troposphere and stratosphere coupling and its hemispheric differences

As already alluded to above, the tropospheric changes are caused by atmosphere circulation changes in the troposphere and above in response to solar forcing. From Fig. 4(a and c), it is seen that the subtropical zonal wind in the troposphere and stratosphere weakens due to the reduction of diabatic heating during both DJF and JJA. Similar wind changes occur in HDUV when the primary solar forcing change is in the stratosphere, and in Smin when the solar forcing change is weak, with smaller magnitudes in both cases (Supporting Information Figure S4). The winter stratospheric wind changes at mid to high latitudes differ significantly between the two hemispheres, with a weak increase (not statistically significant at 95% level) in the NH and a significant decrease in the SH. The former is in apparent contrast to the dynamical responses expected for solar minimum conditions when stratospheric differential heating is reduced and zonal forcing by planetary wave (PW) increases (Kodera & Kuroda, 2002). Further examination of monthly differences shows that the weakening of winter stratospheric wind and its poleward and downward shift from early to late winter, as expected from Kodera and Kuroda (2002); Ineson et al. (2011), are seen in HDUV in both hemispheres and in HD and HDVIR only in the SH (Supporting Information Figure S5), underscoring differences in PW responses to solar forcing changes in the troposphere and in the stratosphere. Hemispheric difference is also seen in the thermal response to solar forcing (From Fig. 4(b and d)). Apart from the general cooling in these simulations expected from reduced solar forcing, there is a weak warming near the tropopause in the NH, and a strong warming that becomes statistically significant around the tropopause in the SH.

These hemispheric differences stem from different PW responses in the two hemispheres (Fig. 4(e-h)). The vertical component of Eliassen-Palm flux (EP_z) shifts equatorward in the troposphere and decreases in the stratosphere (albeit not statistically significant due to the large wave variability during boreal winter) in the NH, and correspondingly the westward forcing by the PWs weakens in the stratosphere. The SH shows the opposite, with both EP_z and wave forcing increasing significantly. This is also seen from the longitudinal and height structures of the meridional wind and temperature (Supporting Information Figure S6), with the wind and temperature changes becoming increasingly out of phase with the climatological zonal wavenumber 1 perturbations in the NH above 30hPa, while in phase in the SH. It is found that PW with zonal wavenumber 1 accounts for most of the hemispheric differences at mid to high latitudes (Supporting Information Figures 7 and 3): it decreases during DJF in NH and increases during JJA and SON in SH in the troposphere and stratosphere. The decrease during boreal winter is consistent with wave 1 increase during a warming climate, which is found to be affected by the subtropical wind and zonally asymmetric diabatic heating changes (Wang & Kushner, 2011). On the other hand, this decrease is likely offset by the weakening of winter stratospheric wind at mid-high latitudes, which tends to increase EP_z of wave 1. Since the subtropical wind changes are similar between the two hemispheres, the wave

1 increase in SH should result mostly from changes of tropospheric wave sources, and it is mutually enhancing with the significant weakening of the winter stratospheric wind. The former is evidenced in Joseph et al. (2004), that the forcing from transients tends to enhance (weaken) wave 1 at high northern (southern) latitudes during winter in a warming climate (thus the opposite in a cooling climate). In contrast to wave 1, PWs with wavenumber 2-4 and 6 increase during both hemispheric winters, and the increase of wave 2-3 extends into the stratosphere.

Comparison of HDVIR and HDUV simulations show that EP_z responses to tropospheric/surface forcing change are opposite for hemispheric winters (Supporting Information Figures 8a, b), while the responses to stratospheric forcing change are similar (Supporting Information Figures 8c, d). The tropospheric/surface forcing and stratospheric forcing are mutually offsetting during boreal winter and enhancing during austral winter. Therefore, the winter stratospheric wind change in HD appears to be less prominent than in HDVIR in the NH, but more prominent than HDVIR and HDUV in the SH (Fig. 4(a,c) and Supporting Information Figures 9a–d).

The PW differences lead to differences in the interplay between dynamical and radiative forcing during hemispheric winters. The decrease of PW forcing in the NH leads to stronger stratospheric winter jet, weaker Brewer-Dobson (BD) circulation, and less adiabatic warming (cooling) in the polar (equatorial) tropopause/stratosphere. The dynamical and radiative effects thus offset each other in the boreal winter stratosphere for zonal wind change, but are mutually enhancing for cooling, as reflected in the magnitude and significance levels of the change. This is exactly the opposite during austral winter, with the dynamical/radiative effects mutually enhancing in decelerating the zonal wind but offsetting in thermal forcing.

4 Summary and Conclusion

While all ESM simulations show larger climate sensitivity than Smin (Table 1), the responses display remarkable general similarities, including the surface temperature, zonal mean states, wave fluxes and structures, and regional climate. Such similarities highlight the robust responses of the climate system to solar forcing change. Solar radiative heating changes in the troposphere and stratosphere both lead to subtropical wind changes that alter the intermediate scale stationary waves and regional climate in the troposphere in a similar way. The responses may not be significant based on statistical sampling when the solar forcing change is nominal, and climate simulations under ESM conditions is thus a valuable tool in exposing the patterns hidden under the large climate variability. Comparisons of HD, HDVIR and HDUV simulations shed light on the underlying mechanisms and elucidate processes where the solar forcing changes in troposphere/surface and stratosphere are mutually enhancing or offsetting. With cooling in both troposphere and middle atmosphere, the ESM simulations also provide a forcing scenario that differs from a warming climate (warming in the troposphere and cooling above).

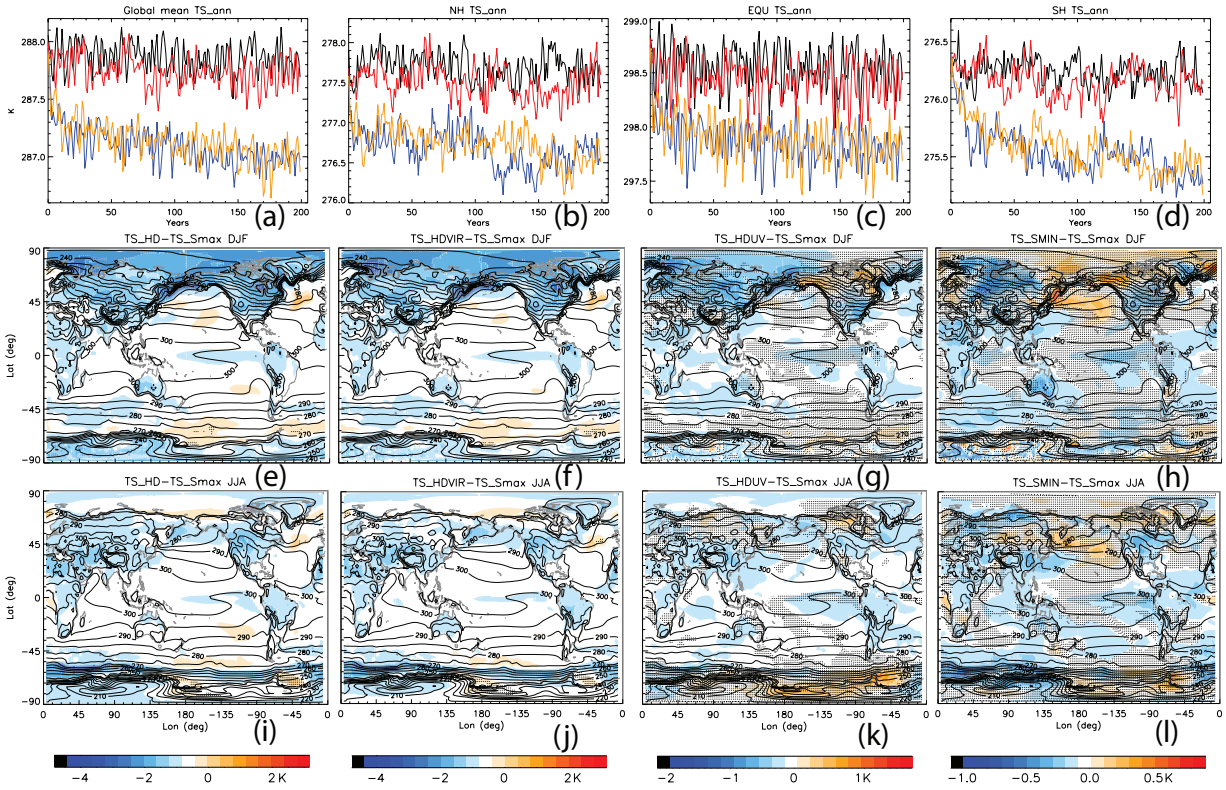

Figure 1: Annually averaged mean surface temperature over (a) the whole globe, (b) northern hemisphere (30°N to the North Pole), (c) tropical region (30°S to 30°N), (d) southern hemisphere (30°S to the South Pole) from Smax (black), HD (blue), HDVIR (orange), and HDUV (red) simulations. Average surface temperature differences (color contours) between years 50-200 of HD, HDVIR, HDUV, and Smin and Smax simulations for DJF (e–h, respectively) and JJA (i–l, respectively). Contour lines are mean temperature from Smax simulations. Unstippled regions are differences that are statistically significant at the 95% level from Student t-test. The white scale in (e-h) corresponds to the averages of the global mean surface temperature change for these cases: cooling by 0.833, 0.79, 0.149, and 0.087K in HD, HDVIR, HDUV, and Smin respectively in comparison with Smax.

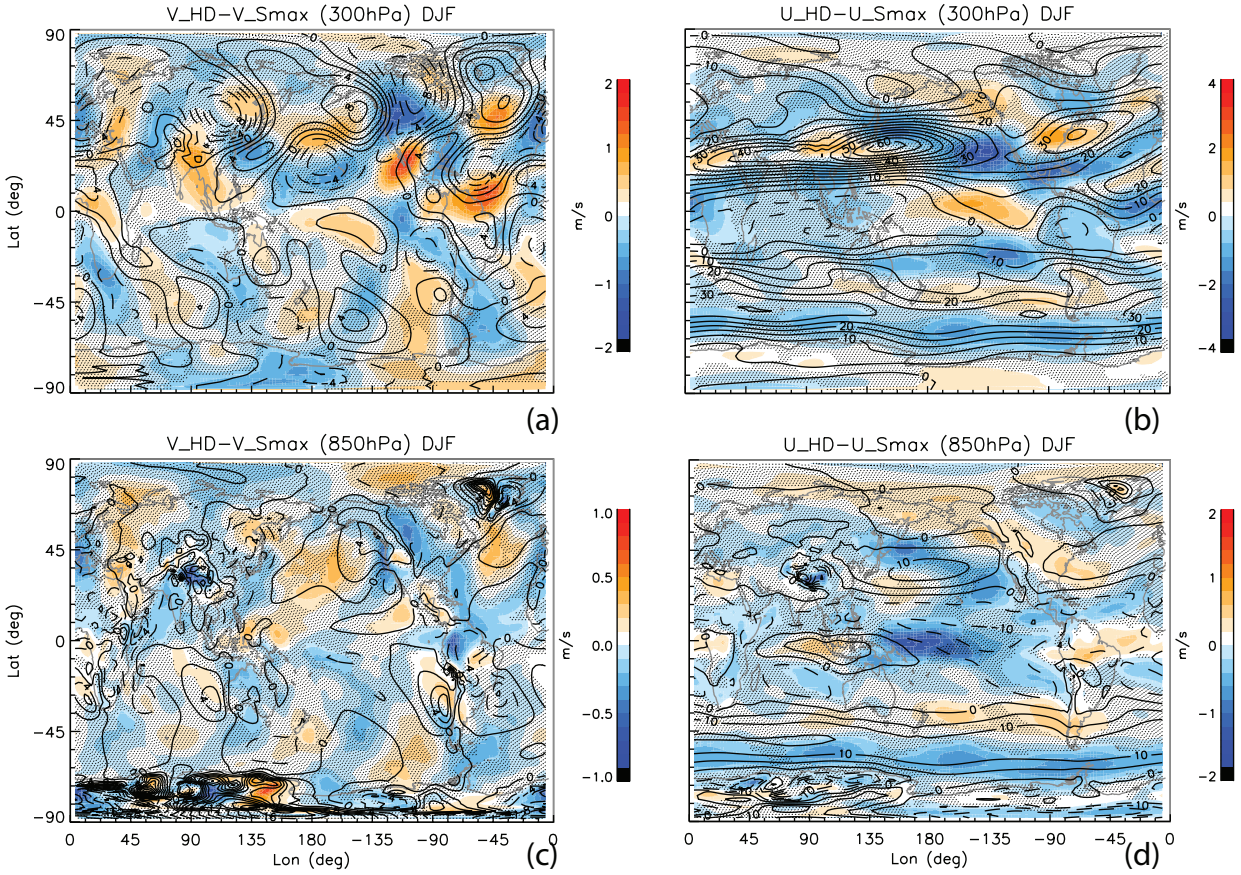

Figure 2: Differences of average (a) meridional wind and (b) zonal wind between 50–200 year of HD and Smax simulations at 300 hPa for boreal winter (DJF). Line contours are average winds (in a, solid: northward (a) and eastward (b), contour intervals: 2ms^{-1} (a) and 2ms^{-1} (b)) from Smax simulations. (c-d): Similar to (a-b), but for 850 hPa.

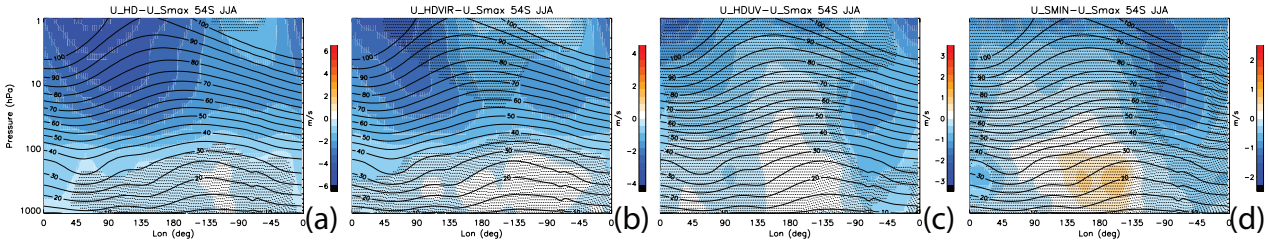

Figure 3: Differences of average zonal wind (color contours) between 50–200 year of (a) HD, (b) HDVIR, (c) HDUV and (d) Smin and Smax simulations at 54°S for austral winter (JJA). Line contours are average zonal wind from Smax simulations (solid: eastward, contour intervals: 5ms^{-1}).

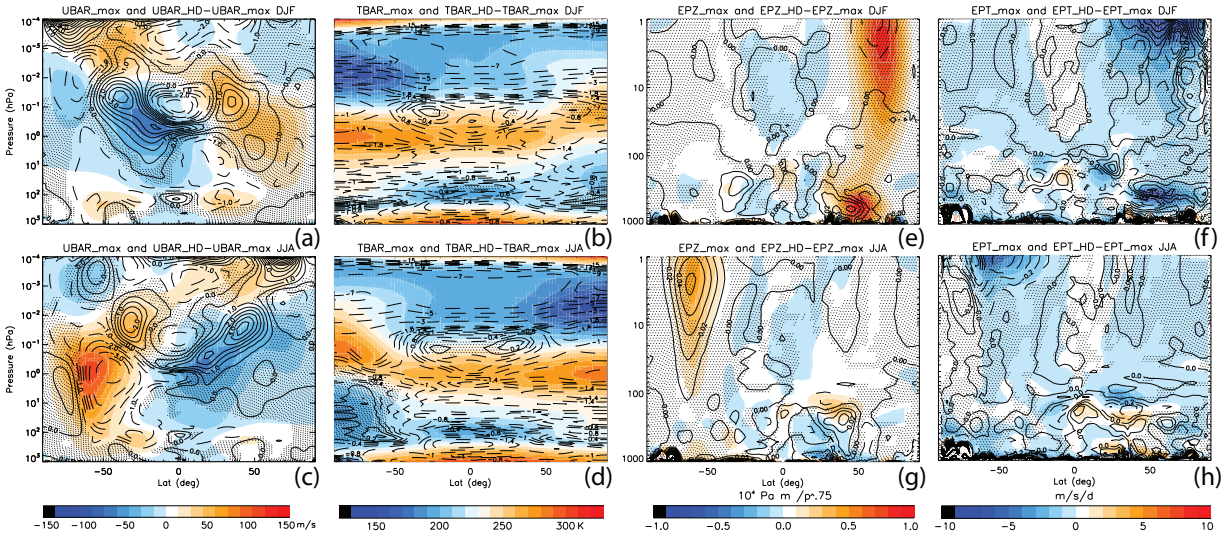

Figure 4: Differences of average zonal mean zonal wind (line contours, solid lines: eastward. Contour interval: 0.5 ms^{-1}) between 50–200 year of HD and Smax simulations for (a) DJF and (c) JJA. Color contours are average zonal mean zonal wind from Smax simulations. (b) and (d): similar to (a) and (c) but for average zonal mean temperature differences (line contour, intervals: 1 K for differences larger than 1K, and 0.2 K for differences less than 1 K). Color contours are average zonal mean temperature from Smax simulations. (e) and (g): similar to (a) and (c) but for average vertical EP flux component differences. The EP flux (unit: Pa m) is normalized by $p^{0.75}$ (p: atmosphere pressure) to better visualize the change at all altitudes (line contour, interval: 0.01×10^4). Color contours are average normalized vertical EP flux component from Smax simulations. (f) and (h): similar to (a) and (c) but for average EP flux divergence differences (line contour, interval: 0.1 $ms^{-1}d^{-1}$). Color contours are average EP flux divergence from Smax simulations.

Solar Forcing Used for Driving CESM/ WACCM Simulations	Nominal solar maximum (Smax)	Nominal solar minimum (Smin)	Non-magnetic, hydrodynamic (HD) reference	SSI(Smin) ($\lambda \leq 320$nm)+ SSI(HD) ($\lambda > 320$nm) (HDVIR)	SSI(HD) ($\lambda \leq 320$nm)+ SSI(Smin) ($\lambda > 320$nm) (HDUV)	Small-scale dynamo with 44G vertical field strength (SSD44)
TSI (Wm^{-2})	1361.93	1360.43	1350.08	1350.84	1359.76	1354.83
Ts (K)	287.87	287.78	287.04	287.08	287.72	287.36
Climate Sensitivity ($K(Wm^{-2})^{-1}$)		0.0578	0.0705	0.0712	0.0691	0.0724

Table 1: CESM/WACCM simulations and the solar forcing used, the corresponding total solar irradiance (TSI), the global mean surface temperature (T_s) averaged over the whole simulation period (Smax) and the last 150 years of the simulations (HD, HDVIR, HDUV, SSD44, and Smin), and the climate sensitivity with respect to Smax.

Acknowledgments

The CESM project is primarily supported by the National Science Foundation (NSF). CESM is a community model and is available for download (https://www.cesm.ucar.edu/models/cesm1.1/index.html) CESM model outputs are served through the Climate Data Gateway (https://www.earthsystemgrid.org/). This material is based on work supported by the National Center for Atmospheric Research (NCAR), which is a major facility sponsored by the NSF under Cooperative Agreement 1852977. Efforts by HLL, MR, SCS and JMM are partially supported by NASA grant NNX16AB82G. High-performance computing support by the NASA Advanced Supercomputing (NAS) Division at Ames Research Center provided by NASA High-End Computing (HEC) Program is acknowledged. We thank I. Simpson for valuable comments, and D. Bailey and A. Altuntas for their help with the sea-ice and ocean model analysis, respectively.

References

Branstator, G. (2002). Circumglobal teleconnections, the jet stream waveguide, and the north atlantic oscillation. *Journal of Climate*, *15*, 1893-1910.

Chiodo, G., Calvo, N., Marsh, D. R., & Garcia-Herrera, R. (2012). The 11 year solar cycle signal in transient simulations from the whole atmosphere community climate model. *Journal of Geophysical Research: Atmospheres*, *117*. doi: 10.1029/2011JD016393

Chiodo, G., Oehrlein, J., Polvani, L. M., Fyfe, J. C., & Smith, A. K. (2019). Insignificant influence of the 11-year solar cycle on the north atlantic oscillation. *Nature Geoscience*, *12*, 94-99. doi: 10.1038/s41561-018-0293-3

da Silva, A., Young, C., & Levitus, S. (1995). *Atlas of surface marine data 1994. Vol.1: Algorithms and procedures* (NOAA Atlas NESDIS No. 6). Washington DC: U.S. Dept. of Commerce, NOAA.

Danabasoglu, G., Bates, S. C., Briegleb, B. P., Jayne, S. R., Jochum, M., Large, W. G., ... Yeager, S. G. (2012). The ccsm4 ocean component. *Journal of Climate*, *25*, 1361-1389. doi: 10.1175/JCLI-D-11-00091.1

Garcia, R. R., Smith, A. K., Kinnison, D. E., Álvaro de la Cámara, & Murphy, D. J. (2017). Modification of the gravity wave parameterization in the whole atmosphere community climate model: Motivation and results. *Journal of the Atmospheric Sciences*, *74*, 275-291. doi: 10.1175/JAS-D-16-0104.1

Gray, L. J., Beer, J., Geller, M., Haigh, J. D., Lockwood, M., Matthes, K., ... White, W. (2010). Solar influences on climate. *Reviews of Geophysics*, *48*. doi: 10.1029/2009RG000282

Gray, L. J., Woollings, T. J., Andrews, M., & Knight, J. (2016). Eleven-year solar cycle signal in the nao and atlantic/european blocking. *Quarterly Journal of the Royal Meteorological Society*, *142*, 1890-1903. doi: 10.1002/qj.2782

Haigh, J. D. (1996). The impact of solar variability on climate. *Science*, *272*, 981-984. doi: 10.1126/science.272.5264.981

Ineson, S., Maycock, A. C., Gray, L. J., Scaife, A. A., Dunstone, N. J., Harder, J. W., ... Wood, R. A. (2015). Regional climate impacts of a possible future grand solar minimum. *Nature Communications*, *6*, 7535. doi: 10.1038/ncomms8535

Ineson, S., Scaife, A. A., Knight, J. R., Manners, J. C., Dunstone, N. J., Gray, L. J., & Haigh, J. D. (2011). Solar forcing of winter climate variability in the northern hemisphere. *Nature Geoscience*, *4*, 753-757. doi: 10.1038/ngeo1282

Joseph, R., Ting, M., & Kushner, P. J. (2004). The global stationary wave response to climate change in a coupled gcm. *J. Climate*, *17*, 540-556.

Kodera, K., & Kuroda, Y. (2002). Dynamical response to the solar cycle. *Journal of Geophysical Research: Atmospheres*, *107*. doi: 10.1029/2002JD002224

Kodera, K., & Shibata, K. (2006). Solar influence on the tropical stratosphere and troposphere in the northern summer. *Geophysical Research Letters*, *33*. doi: 10

.1029/2006GL026659

Marsh, D. R., Garcia, R., Kinnison, D., Boville, B., Sassi, F., & Solomon, S. (2007). Modeling the whole atmosphere response to solar cycle changes in radiative and geomagnetic forcing. *Journal of Geophysical Research*, *112*. doi: 10.1029/2006JD008306

Marsh, D. R., Mills, M. J., Kinnison, D. E., Lamarque, J.-F., Calvo, N., & Polvani, L. M. (2013). Climate Change from 1850 to 2005 Simulated in CESM1(WACCM). *Journal of Climate*, *26*, 7372–7391. doi: 10.1175/JCLI-D-12-00558.1

Matthes, K., Kuroda, Y., Kodera, K., & Langematz, U. (2006). Transfer of the solar signal from the stratosphere to the troposphere: Northern winter. *Journal of Geophysical Research: Atmospheres*, *111*. doi: 10.1029/2005JD006283

Maycock, A. C., Ineson, S., Gray, L. J., Scaife, A. A., Anstey, J. A., Lockwood, M., ... Osprey, S. M. (2015). Possible impacts of a future grand solar minimum on climate: Stratospheric and global circulation changes. *Journal of Geophysical Research: Atmospheres*, *120*, 9043-9058. doi: 10.1002/2014JD022022

Meehl, G. A., Arblaster, J. M., & Marsh, D. R. (2013). Could a future "Grand Solar Minimum" like the maunder minimum stop global warming? *Geophysical Research Letters*, *40*, 1789-1793. doi: 10.1002/grl.50361

Meehl, G. A., Arblaster, J. M., Matthes, K., Sassi, F., & van Loon, H. (2009). Amplifying the pacific climate system response to a small 11-year solar cycle forcing. *Science*, *325*, 1114–1118. doi: 10.1126/science.1172872

Misios, S., Gray, L. J., Knudsen, M. F., Karoff, C., Schmidt, H., & Haigh, J. D. (2019). Slowdown of the walker circulation at solar cycle maximum. *Proceedings of the National Academy of Sciences*, *116*, 7186–7191. doi: 10.1073/pnas.1815060116

Morgenstern, O., Hegglin, M. I., Rozanov, E., O'Connor, F. M., Abraham, N. L., Akiyoshi, H., ... Zeng, G. (2017). Review of the global models used within phase 1 of the chemistry–climate model initiative (ccmi). *Geoscientific Model Development*, *10*, 639–671. doi: 10.5194/gmd-10-639-2017

Rempel, M. (2014, July). Numerical Simulations of Quiet Sun Magnetism: On the Contribution from a Small-scale Dynamo. *Astrophysics Journal*, *789*, 132. doi: 10.1088/0004-637X/789/2/132

Rempel, M. (2018, June). Small-scale Dynamo Simulations: Magnetic Field Amplification in Exploding Granules and the Role of Deep and Shallow Recirculation. *Astrophysics Journal*, *859*, 161. doi: 10.3847/1538-4357/aabba0

Rempel, M. (2020). On the contribution of quiet Sun magnetism to solar irradiance variations: Constraints on quiet Sun variability and grand minimum scenarios. *Astrophysical Journal*, *894*. doi: 10.3847/1538-4357/ab8633

Schrijver, C. J., Livingston, W. C., Woods, T. N., & Mewaldt, R. A. (2011). The minimal solar activity in 2008–2009 and its implications for long-term climate modeling. *Geophysical Research Letters*, *38*. doi: 10.1029/2011GL046658

Shapiro, A. I., Schmutz, W., Rozanov, E., Schoell, M., Haberreiter, M., Shapiro, A. V., & Nyeki, S. (2011). A new approach to the long-term reconstruction of the solar irradiance leads to large historical solar forcing. *Astrophysics Journal*, *529*, A67. doi: 10.1051/0004-6361/201016173

Simpson, I. R., Seager, R., Ting, M., & Shaw, T. A. (2016). Causes of change in northern hemisphere winter meridional winds and regional hydroclimate. *Nature Climate Change*, *6*, 65–70. doi: 10.1038/nclimate2783

Théblemont, R., Matthes, K., Omrani, N.-E., Kodera, K., & Hansen, F. (2015). Solar forcing synchronizes decadal north atlantic climate variability. *Nature Communications*, *6*, 8268. doi: 10.1038/ncomms9268

Tilmes, S., Lamarque, J.-F., Emmons, L. K., Kinnison, D. E., Marsh, D., Garcia, R. R., ... Blake, N. (2016). Representation of the community earth system model (cesm1) cam4-chem within the chemistry-climate model ini-

tiative (ccmi). *Geoscientific Model Development*, *9*, 1853–1890. doi: 10.5194/gmd-9-1853-2016

Vögler, A., & Schüssler, M. (2007, April). A solar surface dynamo. *Astronomy and Astrophysics*, *465*, L43-L46. doi: 10.1051/0004-6361:20077253

Wang, L., & Kushner, P. J. (2011). Diagnosing the stratosphere-troposphere stationary wave response to climate change in a general circulation model. *Journal of Geophysical Research: Atmospheres*, *116*. doi: https://doi.org/10.1029/2010JD015473

Wegner, T., Kinnison, D. E., Garcia, R. R., & Solomon, S. (2013). Simulation of polar stratospheric clouds in the specified dynamics version of the whole atmosphere community climate model. *Journal of Geophysical Research: Atmospheres*, *118*, 4991-5002. doi: 10.1002/jgrd.50415

Wills, R. C. J., White, R. H., & Levine, X. J. (2019). Northern hemisphere stationary waves in a changing climate. *Current Climate Change Reports*, *5*, 372–389. doi: 10.1007/s40641-019-00147-6